



An efficient adaptive algorithm for photon-electron coupled Boltzmann equation in radiation therapy

Xilin Zhang^a, Peimeng Yin^b, Xue Hong^c, Wei Wu^c, Wangyao Li^c, Yuxin Wang^d, Yan Xu^{ID a,*}, Hao Gao^c

^a School of Mathematical Sciences, University of Science and Technology of China, Hefei, Anhui, China

^b Department of Mathematical Sciences, The University of Texas at El Paso, USA

^c Department of Radiation Oncology, University of Kansas Medical Center, USA

^d School of Nuclear Science and Technology, University of Science and Technology of China, Hefei, Anhui, China

ARTICLE INFO

Keywords:

Radiation transport
Photon-electron coupled Boltzmann equation
Radiotherapy
Discontinuous Galerkin methods
Adaptive algorithm

ABSTRACT

In this paper, we propose an efficient adaptive algorithm for the photon-electron coupled Boltzmann equations in radiation therapy. The algorithm employs adaptive mesh technologies for both angular and spatial discretization and effectively solves the equation across various domains with a reduced number of degrees of freedom and computational time while maintaining accuracy. For spatial discretization, we employ an adaptive discontinuous Galerkin scheme based on material redefinition to automatically conduct adaptive refinement during the computation process. For angular discretization, we utilize high-order discretization near the incident direction, while low-order discretization is applied to other directions. We compare its performance with the classical Monte Carlo simulations for both mono-energetic and multi-energetic photon beams in various media. Numerical results demonstrate the efficiency and accuracy of the algorithm.

1. Introduction

The transport process refers to the random statistical motion of particles caused by irregular collisions with nuclei, forming the basis of transport theory [1]. This theory is widely applied to describe the transport processes of neutrons, photons, electrons, and molecules within a medium, as well as to study the non-equilibrium statistical behavior of large particle populations. Our study focuses on the application of transport theory in radiation therapy, a primary cancer treatment that benefits approximately 50 % of cancer patients [2], with photon radiation therapy being the most commonly used method in clinical practice. High-energy particles are delivered to the tumor target area via an external radiation source to eradicate the tumor. However, these particles can also inflict significant radiation-induced damage on surrounding healthy tissues, potentially imposing life-threatening risks. Therefore, it is crucial to accurately calculate the dose distribution within the body to maximize tumor destruction while minimizing harm to adjacent normal tissues.

The particle transport process in radiation therapy is mathematically described by the linear Boltzmann transport (LBT) equation, an integro-differential equation governing flux density. A widely used method for solving this equation is the Monte Carlo (MC) algorithm, which can provide highly accurate solutions for arbitrary geometries. However, the MC algorithm's extensive computation times, especially for complex geometries, can limit its clinical applicability. An alternative approach is to solve the LBT equation deterministically by discretizing variables such as space (using finite difference or finite element methods), angle (using discrete ordinates), and energy (using multigroup techniques). Deterministic methods offer faster solutions within the computational domain,

* Corresponding author.

E-mail address: yxu@ustc.edu.cn (Y. Xu).

facilitating accurate dose distribution. In recent years, these methods [3,4] have taken more attention for their efficiency. Additionally, significant research has focused on particle transport processes influenced by magnetic fields, with notable contributions by Aubin et al. [5–9]. These studies further expand the understanding and potential applications of transport theory in radiation therapy.

In this work, we employ discontinuous Galerkin (DG) methods for the spatial discretization of the photon-electron coupled Boltzmann equation. DG methods are particularly effective for handling complex boundary conditions and mesh adaptation, enabling a significant reduction in the degrees of freedom of the discrete LBT system. Previous works have demonstrated DG methods in similar LBT models: Decaria et al. [10] applied DG method on the linear Boltzmann semiconductor model. Ghattassi et al. [11] used it to solve the nonlinear radiative-conductive heat transfer systems. Han [12] et al. study discrete-ordinate discontinuous Galerkin methods for solving the radiative transfer equation. Houston et al. [13] introduce an hp-version discontinuous Galerkin finite element method for the linear Boltzmann transport problem.

In this paper, we propose a novel algorithm for solving the photon-electron coupled Boltzmann equation, leveraging adaptive mesh technology for both angular and spatial discretization. The resulting scheme achieves efficient solutions across diverse domains enabling to minimize the degrees of freedom while maintaining high accuracy. Our results demonstrate excellent agreement between the benchmark and our proposed algorithm. For regions where the dose exceeds 10% of the maximum dose, gamma indices [14] achieve at least 92% and 95% under 2%/2 mm and 2%/3 mm DTA criteria, respectively, for all test models. The key highlights of this study are centered as follows:

1. An adaptive DG scheme based on material redefinition is proposed to automatically conduct adaptive refinement during the computation process. This adaptive approach is entirely objective.
2. An adaptive technique is applied to angular discretization, utilizing high-order discretization near the incident directions and low-order discretization for other directions.

The outline of this manuscript is organized as follows: Section 2 presents the equation to be solved and some basic processing before discretization. Detailed discretization methods are introduced in Section 3. In Section 4, numerical examples are shown to demonstrate the efficiency of our algorithm. Finally, the conclusion and outlook are given in Section 5.

2. Model equations

In photon transport, the photon-electron coupled linear Boltzmann transport equations for solving flux densities of photons and electrons, $\psi^\gamma(\vec{r}, E, \hat{\Omega})$ and $\psi^e(\vec{r}, E, \hat{\Omega})$, are given by

$$\begin{cases} \hat{\Omega} \cdot \nabla \psi^\gamma(\vec{r}, E, \hat{\Omega}) + \sigma_t^\gamma(\vec{r}, E) \psi^\gamma(\vec{r}, E, \hat{\Omega}) = q^{\gamma\gamma}(\vec{r}, E, \hat{\Omega}) + S(\vec{r}, E, \hat{\Omega}), \vec{r} \in D, \\ \hat{\Omega} \cdot \nabla \psi^e(\vec{r}, E, \hat{\Omega}) + \sigma_t^e(\vec{r}, E) \psi^e(\vec{r}, E, \hat{\Omega}) = q^{ee}(\vec{r}, E, \hat{\Omega}) + q^{\gamma e}(\vec{r}, E, \hat{\Omega}), \vec{r} \in D, \\ \psi^\gamma(\vec{r}, E, \hat{\Omega}) = 0, \psi^e(\vec{r}, E, \hat{\Omega}) = 0, \text{ on } \partial D^- = \{\vec{r} : \vec{n}(\vec{r}) \cdot \hat{\Omega} < 0\}, \end{cases} \quad (1)$$

with

$$q^{p_1 p_2}(\vec{r}, E, \hat{\Omega}) = \int_0^\infty dE' \int_{4\pi} \sigma_s^{p_1 p_2}(\vec{r}, E' \rightarrow E, \hat{\Omega} \cdot \hat{\Omega}') \psi^{p_1}(\vec{r}, E', \hat{\Omega}') d\hat{\Omega}',$$

where $p_1, p_2 = \gamma, e$, the notation \vec{r} is a point in 3D Euclidean space D , energy E moving in direction $\hat{\Omega} = (\mu, \eta, \xi)$ whose three components are the direction cosines of x -, y - and z -axes. Other functions are as follows:

- $\vec{n}(\vec{r})$ is the outward normal unit vector field for a point $\vec{r} \in \partial D$;
- $\sigma_t^{p_1}(\vec{r}, E)(p_1 = \gamma, e)$ is macroscopic total cross section;
- $\sigma_s^{p_1 p_2}(\vec{r}, E' \rightarrow E, \hat{\Omega} \cdot \hat{\Omega}')(p_1, p_2 = \gamma, e)$ is macroscopic differential scattering cross section;
- $q^{p_1 p_2}(\vec{r}, E, \hat{\Omega})(p_1, p_2 = \gamma, e)$ is the scattering term between different particles;
- $S(\vec{r}, E, \hat{\Omega})$ is the external photon source term.

Since the two equations in Eq. (1) have very similar forms ($q^{\gamma e}$ can be considered as the source term of electron transport), the same numerical methods will be used in two equations. For presentation convenience and symbol clarity, the superscript γ, e will be omitted in the subsequent section when there is no ambiguity, and all following ψ can denote any one of ψ^γ and ψ^e , the same is true for the other variable, such as σ_t .

We will not exactly solve Eq. (1) because at the right end of Eq. (1), there is an integral about $\hat{\Omega}$ over the unit sphere, which is difficult to solve directly. To overcome it, Legendre expansion is applied on integration about angular variable $\hat{\Omega}$ in Eq. (1), and the scattering term $q(\vec{r}, E, \hat{\Omega})$ becomes

$$q(\vec{r}, E, \hat{\Omega}) = \sum_{l=0}^{\infty} \int dE' \sigma_{sl}(\vec{r}, E' \rightarrow E) \sum_{m=-l}^l Y_{lm}^*(\hat{\Omega}) \times \int d\hat{\Omega}' Y_{lm}(\hat{\Omega}') \psi(\vec{r}, E', \hat{\Omega}'),$$

where $\sigma_{sl}(\vec{r}, E' \rightarrow E)$ is Legendre coefficient, and $Y_{lm}(\hat{\Omega})$ is sphere harmonic function while $Y_{lm}^*(\hat{\Omega})$ is its complex conjugation. Further, we set the real and imaginary parts of $Y_{lm}(\hat{\Omega})$ are $Y_{lm}^e(\hat{\Omega})$ and $Y_{lm}^o(\hat{\Omega})$ respectively, i.e.,

$$Y_{lm}(\hat{\Omega}) = Y_{lm}^e(\hat{\Omega}) + i Y_{lm}^o(\hat{\Omega}),$$

and the scalar moment is

$$\phi_{lm}^k(\vec{r}, E) = \int d\hat{\Omega}' Y_{lm}^k(\hat{\Omega}') \psi(\vec{r}, E, \hat{\Omega}'), \quad k \in \{e, o\}. \quad (2)$$

When considering the properties of $Y_{lm}(\hat{\Omega})$, Eq. (1) has format as follows:

$$\begin{aligned} & \hat{\Omega} \cdot \nabla \psi(\vec{r}, E, \hat{\Omega}) + \sigma_t(\vec{r}, E) \psi(\vec{r}, E, \hat{\Omega}) \\ &= S(\vec{r}, E, \hat{\Omega}) + \sum_{l=0}^{\infty} \sum_{m=0}^l (2 - \delta_{m0}) \int dE' \sigma_{sl}(\vec{r}, E' \rightarrow E) \sum_{k \in \{e, o\}} Y_{lm}^k(\hat{\Omega}) \phi_{lm}^k(\vec{r}, E'). \end{aligned} \quad (3)$$

Notice that there is a summation from 0 to ∞ at the right end of Eq. (3), which is clearly unachievable, so numerical truncation is utilized and only the first L terms that dominate the summation are considered.

3. Numerical discretization

3.1. Angular adaptive discretization

In the LBT equation, there is an integral operator about angles in the unit sphere. So in angular discretization, we need to find the angular discrete abscissas over the unit sphere and their corresponding weights. If we select a quadrature with N points $\{\hat{\Omega}_n\}_{n=1}^N$ and corresponding weights $\{w_n\}_{n=1}^N$, then scalar moments in Eq. (2) can be approximated by

$$\phi_{lm}^k(\vec{r}, E) \approx \sum_{n=1}^N w_n Y_{lm}^k(\hat{\Omega}_n) \psi(\vec{r}, E, \hat{\Omega}_n), \quad k \in \{e, o\}.$$

3.1.1. The classical S_N method

The most usual angular discretization method is the S_N method. It discretizes the entire sphere into completely symmetric $N(N+2)$ discrete points and sets different weights to each point to ensure the accuracy of numerical integration on the sphere. For any incident angle, the S_N method uses the same discretization angle quadrature. However, when the incident angle isn't in the quadrature, S_N method cannot approximate the integral of the source term well, which introduces an inevitable computational error in the subsequent calculation. The only thing S_N method for reducing error is to increase N in order to refine the angular quadrature. When N increases, instead of refining directly based on the original quadrature, the S_N method re-finds points on the entire unit sphere. Thus in some cases, increasing N may not reduce the error introduced by angular discretization and might increase it. The degrees of freedom of the whole system increase by roughly N^2 order, which is highly impractical.

3.1.2. The adaptive Lobatto–Tschebyscheff method

We introduce a new adaptive angular discretization “Lobatto–Tschebyscheff” method ($L – T$ method) which selects n different ξ levels by Gauss–Lobatto quadrature and then selects different μ values by Tschebyscheff quadrature at each ξ level. In the first octant, surface integration on the unit sphere is accomplished by

$$A = \frac{2}{\pi} \int_0^1 d\xi \int_0^{\pi/2} d\omega \quad (4)$$

with ω defined through $\eta = \sqrt{1 - \xi^2} \sin \omega$ and $\mu = \sqrt{1 - \xi^2} \cos \omega$. Then

$$A = \frac{2}{\pi} \int_0^1 d\xi \int_0^{\sqrt{1-\xi^2}} \frac{d\mu}{\sqrt{1 - \mu^2 - \xi^2}} = \frac{2}{\pi} \int_0^1 d\xi \int_0^1 \frac{dy}{\sqrt{1 - y}} \quad (5)$$

with $\mu = \sqrt{1 - \xi^2} y$. This suggests that the y integration be accomplished by the Tschebyscheff quadrature and the ξ integration by the Legendre quadrature. In angle space, the incident direction is the most special one, the flux $\psi^y(\vec{r}, E, \hat{\Omega})$ is larger near incident direction $\hat{\Omega}_0 = (\mu_0, \eta_0, \xi_0)$ than elsewhere. Thus in discretization, the incident angle should be selected first and more discretization angles should be selected near $\hat{\Omega}_0$ while fewer angles elsewhere. The angular discretization is outlined in Algorithm 1.

Algorithm 1 has the following advantage compared with the classical S_N scheme:

- For any incident angle, the discrete quadrature can include it as accurately as possible to make the error introduced by angular discretization smaller.
- The refinement of angular quadrature can be done directly based on the original quadrature to ensure that for any incident angle, the refinement allows error introduced by the angular discretization to be reduced.
- The quadrature refinement can be performed locally, rather than over the entire unit sphere as in S_N method, to allow for less increase in degrees of freedom due to quadrature refinement while maintaining accuracy. Only at ξ_0 level, higher order Tschebyscheff quadrature is used for less error in angular discretization and at other ξ levels, low order Tschebyscheff quadrature is enough.
- As N increases, the degrees of freedom of the whole system remain almost unchanged, which effectively remedies the shortcomings of the S_N method.
- The new method does not require complete symmetry as S_N method.

Remark 3.1. In the following paper, the $L – T(N)$ method denotes the selection of N points for angular discretization quadrature.

Algorithm 1: Lobatto–Tschebyscheff angular discretization method.

Input: incident direction (μ_0, η_0, ξ_0) ;

Set $0 < \xi_0 < 1$; Divide $[-1, 1]$ into $[-1, -\xi_0]$, $[-\xi_0, \xi_0]$ and $[\xi_0, 1]$;

for $j = 1, 2, 3$ **do**

Utilize Gauss Lobatto quadrature on j th sub-interval above; Get ξ abscissas $\{\xi_{ij}\}_{ij=1}^{N_j}$ and corresponding weights $\{w_{ij}\}_{ij=1}^{N_j}$;

Combine three sub-sequences $\{\xi_{i1}\}_{i1=1}^{N_1}$, $\{\xi_{i2}\}_{i2=1}^{N_2}$, $\{\xi_{i3}\}_{i3=1}^{N_3}$ and weights $\{w_{i1}\}_{i1=1}^{N_1}$, $\{w_{i2}\}_{i2=1}^{N_2}$, $\{w_{i3}\}_{i3=1}^{N_3}$;

Denote them as $\{\xi_i\}_{i=1}^N$ and $\{w_i\}_{i=1}^N$;

for $i = 1, 2, \dots, N$ **do**

Find μ abscissas and point weights on ξ_i level by Tschebyscheff quadrature:

$$\mu_{ik} = \cos\left(\frac{2n_i - 2k - 1}{2n_i}\right), \quad p_i = \frac{w_i}{n_i};$$

Get η abscissas by $\eta = \pm\sqrt{1 - \xi^2 - \mu^2}$;

Output: Angular discretization quadrature $\{(\mu_{ik}, \pm\eta_{ik}, \xi_i)\}_{(i,k)=1}^{(N,n_i)}$.

3.2. Energy discretization

As for energy variables, the multi-group method is used for discretization. Firstly, two energy values $E_G = 0$ and E_0 which are big enough to ignore particles with higher energy are chosen respectively and then divide the energy spectrum into G intervals. Finally, Eq. (3) in group g for angle $\hat{\Omega}_n$

$$\begin{aligned} \hat{\Omega}_n \cdot \nabla \psi_g(\vec{r}, \hat{\Omega}_n) + \sigma_g(\vec{r}) \psi_g(\vec{r}, \hat{\Omega}_n) \\ = S_g(\vec{r}, \hat{\Omega}_n) + \sum_{l=0}^{\infty} \sum_{m=0}^l (2 - \delta_{m0}) \sum_{g'=1}^G \sigma_{lgg'}(\vec{r}) \sum_{k \in \{e,o\}} Y_{lm}^k(\hat{\Omega}_n) \phi_{lmg'}^k(\vec{r}), \quad g = 1, 2, \dots, G, \end{aligned} \quad (6)$$

where

$$\psi_g(\vec{r}, \hat{\Omega}) = \psi(\vec{r}, E, \hat{\Omega})/f(E), \quad \sigma_g(\vec{r}) = \int_g dE \sigma_t(\vec{r}, E) f(E), \quad S_g(\vec{r}, \hat{\Omega}) = \int_g dE S(\vec{r}, E, \hat{\Omega}),$$

$$\sigma_{lgg'}(\vec{r}) = \int_g dE \int_{g'} dE' \sigma_{sl}(\vec{r}, E' \rightarrow E) f(E'), \quad \phi_{lmg}^k(\vec{r}) = \sum_{n=1}^N w_n Y_{lm}^k(\hat{\Omega}_n) \psi_g(\vec{r}, \hat{\Omega}_n), \quad k \in \{e,o\},$$

and $f(E)$ is a characterization function supported on group g and is usually set to $1/(E_{g-1} - E_g)$.

3.3. Spatial adaptive discretization

3.3.1. DG methods

The DG finite element method is used to solve multigroup discrete-ordinates linear Boltzmann transport equations on adaptive hexahedral elements.

In three dimension domain D , the LBT equation in group g and angle $\hat{\Omega}_n = (\mu_n, \eta_n, \xi_n)$ has format as follows:

$$\begin{cases} \left[\hat{\Omega}_n \cdot \nabla + \sigma_g(x, y, z) \right] \psi_g(\vec{r}, \hat{\Omega}_n) = q_g(\vec{r}, \hat{\Omega}_n), \quad \vec{r} \in D, \\ \psi_g(\vec{r}, \hat{\Omega}_n) = 0, \text{ on } \partial D^- = \{\vec{r} : \vec{n}(\vec{r}) \cdot \hat{\Omega}_n < 0\}, \end{cases} \quad (7)$$

where

$$\hat{\Omega}_n \cdot \nabla = \mu_n \frac{\partial}{\partial x} + \eta_n \frac{\partial}{\partial y} + \xi_n \frac{\partial}{\partial z},$$

$$q_g(\vec{r}, \hat{\Omega}_n) = S_g(\vec{r}, \hat{\Omega}_n) + \sum_{l=0}^{\infty} \sum_{m=0}^l (2 - \delta_{m0}) \sum_{g'=1}^G \sigma_{lgg'}(\vec{r}) \sum_{k \in \{e,o\}} Y_{lm}^k(\hat{\Omega}_n) \phi_{lmg'}^k(\vec{r}).$$

For symbol simplicity, we will omit variable dependencies for functions in this subsection. Let \mathcal{T}_h is a partition of D , consisting of hexahedrons. The finite element space is

$$V_h \triangleq \{v : v \in L^2(D), v|_K \in Q^k(K), \forall K \in \mathcal{T}_h\},$$

where Q_k is k th order polynomial space in each direction. Then the DG approximation for Eq. (7) reads: find $\psi_g \in V_h$ such that

$$\sum_{K \in \mathcal{T}_h} \left[\int_{\partial K} \psi_g^- v^{\text{int}} \hat{\Omega}_n \cdot \vec{n} d\sigma - \int_K \psi_g \hat{\Omega}_n \cdot \nabla v + \int_K \sigma_g \psi_g v \right] = \sum_{K \in \mathcal{T}_h} \int_K q_g v. \quad (8)$$

The boundary numerical flux over each element face is defined as

$$\psi_g^-(\vec{r}, \hat{\Omega}_n) = \begin{cases} \psi_g^{\text{inc}}(\vec{r}, \hat{\Omega}_n), & \vec{n} \cdot \hat{\Omega}_n < 0, \\ \psi_g(\vec{r}, \hat{\Omega}_n), & \vec{n} \cdot \hat{\Omega}_n \geq 0, \end{cases}$$

where \vec{n} is the unit normal vector of element face and ψ_g^{inc} represents incoming angular flux from the upstream element through the face ∂K .

Remark 3.2. The basis functions for the DG method are typically chosen as k th order polynomials, which provide a numerical solution to the LBT equation with $k + 1$ order accuracy relative to the mesh size h . However, due to the high degrees of freedom in the overall system, only linear polynomials are used as basis functions in the examples presented in this paper.

Remark 3.3. Due to the assumption of discontinuity in the approximate solution, the DG method requires less mesh regularity and can be refined or coarsened without continuity constraints. Additionally, different elements of the mesh can be approximated using varying forms of polynomial approximations with different orders. This flexibility facilitates the creation of adaptive meshes.

3.3.2. Adaptive spatial mesh

In this paper, we utilize an adaptive hexahedral mesh to partition the computational domain. In practical applications, the computational domain can become complex, with each voxel potentially surrounded by others containing different materials. To accurately calculate the dose distribution for each voxel in phase space, it is essential to use a relatively small spatial mesh size (e.g., $2 \text{ mm} \times 2 \text{ mm} \times 2 \text{ mm}$). However, employing a uniform $2 \text{ mm} \times 2 \text{ mm} \times 2 \text{ mm}$ voxel size across the entire region would result in over 3 million spatial degrees of freedom for a simulation area of $30 \text{ cm} \times 30 \text{ cm} \times 30 \text{ cm}$, making calculations nearly infeasible. Additionally, using such a dense mesh in regions where material properties remain constant or energy levels are low would waste computational resources.

To address these challenges in simulations of complex models, we implement an adaptive mesh technique. This approach dynamically adjusts the mesh size based on material distribution and the characteristics of the physical field, effectively reducing the computational burden while maintaining accuracy. In spatial discretization, areas where the flux $\psi(\vec{r}, E, \hat{\Omega})$ exhibits significant changes are particularly important to note. In radiotherapy, these areas correspond to the boundary of the incident beam and the interfaces between different materials. To capture these variations effectively, a coarser rectangular mesh will be used to divide the computational domain, and the material of each element will be identified based on its Hounsfield unit (HU) value. For each element, we will compare its material with those of its neighbors in the x , y , and z directions. If any differences are detected, the element will be refined in the corresponding direction. Special attention must also be given to the position of the incident beam. At the boundary of the incident beam field, dose distribution can vary significantly on either side due to the large intensity gradient of the beam. Consequently, it is essential to refine the voxels on both sides of the incident beam edge. Finally, the materials of all elements will be re-evaluated after refinement to ensure accuracy. The process for constructing the adaptive mesh is summarized in [Algorithm 2](#).

3.4. Source iteration

Due to the large degrees of freedom in the discrete LBT equation, it cannot be solved directly. Instead, approximate solutions are typically obtained using iterative methods, with the source iteration method being one of the most commonly used approaches. Since particles will never scatter to higher energy from low energy, [Eq. \(6\)](#) can be rewritten as

$$\begin{aligned} \hat{\Omega}_n \cdot \nabla \psi_g(\vec{r}, \hat{\Omega}_n) + \sigma_g(\vec{r}) \psi_g(\vec{r}, \hat{\Omega}_n) \\ = s_g(\vec{r}, \hat{\Omega}_n) + \sum_{l=0}^{\infty} \sum_{m=0}^l (2 - \delta_{m0}) \sigma_{lgg}(\vec{r}) \sum_{k \in \{e,o\}} Y_{lm}^k(\hat{\Omega}_n) \phi_{lmg}^k(\vec{r}), \quad g = 1, 2, \dots, G, \end{aligned} \quad (9)$$

where

$$s_g(\vec{r}, \hat{\Omega}_n) = \sum_{g' < g} \sum_{l=0}^{\infty} \sum_{m=0}^l (2 - \delta_{m0}) \sigma_{lgg'}(\vec{r}) \sum_{k \in \{e,o\}} Y_{lm}^k(\hat{\Omega}_n) \phi_{lmg'}^k(\vec{r}) + S_g(\vec{r}, \hat{\Omega}_n).$$

Then for energy group g and angle $\hat{\Omega}_n$, initial value is set to $\psi_g^0 = 0$ and i th iteration ψ_g^i is implemented as follows:

$$\begin{aligned} [\hat{\Omega}_n \cdot \nabla + \sigma_g(\vec{r})] \psi_g^i(\vec{r}, \hat{\Omega}_n) &= \sum_{l=0}^{\infty} \sum_{m=0}^l (2 - \delta_{m0}) \sigma_{lgg}(\vec{r}) \sum_{k \in \{e,o\}} Y_{lm}^k(\hat{\Omega}_n) \phi_{lmg}^{k,i-1}(\vec{r}) + s_g(\vec{r}, \hat{\Omega}_n), \\ g &= 1, 2, \dots, G, \quad i = 1, 2, \dots, l+1, \end{aligned}$$

where

$$\phi_{lmg}^{k,i}(\vec{r}) = \sum_{n=1}^N w_n Y_{lm}^k(\hat{\Omega}_n) \psi_g^i(\vec{r}, \hat{\Omega}_n), \quad k \in \{e,o\}.$$

Algorithm 2: Adaptive spatial discretization method.

Input: ① CT image of computation domain,
 ② Incident beam intensity $\psi^{in}(\vec{r}, E, \hat{\Omega})$,
 ③ Conversion table T from Hounsfield units to material properties;

Step 1: Initialize mesh

Divide computation domain into uniform hexahedral mesh $\mathcal{T}_{\text{coarse}}$;

Define null material matrix $\mathbf{M} \in \mathbb{R}^{N_x \times N_y \times N_z}$, where N_x, N_y, N_z is the number of elements via x-, y-, z- direction in $\mathcal{T}_{\text{coarse}}$.

foreach K in $\mathcal{T}_{\text{coarse}}$ **do**

 Calculate average Hounsfield unit value of K ;

 Get material property of K from Table T and write it to \mathbf{M} .

Step 2: Heterogeneous adaptive refinement

foreach K in $\mathcal{T}_{\text{coarse}}$ **do**

for d in {x, y, z} **do**

if $\mathbf{M}(K) \neq \mathbf{M}(\text{neighboring voxels of } K \text{ in } d - \text{ direction})$ **then**

 Split K into several smaller voxels along d -direction.

Denote mesh $\mathcal{T}_{\text{coarse}}$ after heterogeneous adaptive refinement as $\mathcal{T}_{\text{Heterogeneous}}$.

Step 3: High gradient adaptive refinement

Calculate partial derivatives of ψ^{in} everywhere on computation domain;

Denote average value of $\partial_x \psi^{in}, \partial_y \psi^{in}$ and $\partial_z \psi^{in}$ over all computation domain as m_x, m_y and m_z , respectively.

foreach K in $\mathcal{T}_{\text{Heterogeneous}}$ **do**

for d in {x, y, z} **do**

if $\partial_d \psi^{in}|_K > m_d$ **then**

 Split K into several smaller voxels along d -direction.

Denote mesh $\mathcal{T}_{\text{Heterogeneous}}$ after heterogeneous adaptive refinement as $\mathcal{T}_{\text{refine}}$.

Step 4: Material redefinition

Redefine null material matrix \mathbf{M} with the same size as $\mathcal{T}_{\text{refine}}$.

foreach K in $\mathcal{T}_{\text{refine}}$ **do**

 Calculate average Hounsfield unit value of K ;

 Get material property of K from Table T and write it to \mathbf{M} .

Output: Adaptive mesh $\mathcal{T}_{\text{refine}}$ and material matrix \mathbf{M} .

4. Numerical results

In this section, we present various experimental results. The cross sections needed in this Section are all generated by the coupled electron-photon cross section generating code (CEPXS) [15]. The reference solutions in all test cases are simulated by MC method with $1 \times 1 \times 1 \text{ mm}^3$ voxels. To highlight the advantages of our algorithm over the MC algorithm across multiple dimensions, we recalculated the dose distribution using the MC algorithm on the same grid as the linear Boltzmann transport (LBT) model in both scenarios. First, a numerical model is employed to validate the accuracy and convergence order. Next, we demonstrate the efficiency of material redefinition in spatial adaptive discretization. Finally, we compare our algorithm against the MC method with the same mesh for different application models.

4.1. Convergence test

First, we use a numerical model to verify the convergence order in spatial discretization. In this model, we consider a one-group problem, setting both the total cross-section and the scattering cross-section to isotropic for simplicity. The details of the model parameters are presented Table 1. In $L - T(50)$, 5th order Lobatto quadrature is selected as ξ level, and 4,6,7,6,4th order Tschebyshev quadrature is selected for each ξ level.

To verify the convergence of the code, we choose angular flux ψ with exact solution

$$\psi(\vec{r}, E, \hat{\Omega}) = \sin(x + y + z).$$

The slices of the exact solution ψ are as in Fig. 1. The boundary condition is

$$\psi|_{\partial D^-} = \sin(x + y + z), \text{ on } \vec{n} \cdot \hat{\Omega} < 0$$

and the corresponding extra source is

$$S(\vec{r}, E, \hat{\Omega}) = (\mu + \eta + \xi) \cos(x + y + z) + \sin(x + y + z).$$

Table 1
Details in numerical model.

Parameters	Values
Computation domain	$[-1, 1] \times [-1, 1] \times [-1, 1]$
Angular discrete quadrature	$L = T(50)$
Legendre expansion number	$L = 5$
Total cross section	$\sigma_t(\vec{r}, E) = 2$
Scattering cross section	$\sigma_s(\vec{r}, E' \rightarrow E, \hat{\Omega} \cdot \hat{\Omega}') = 1$

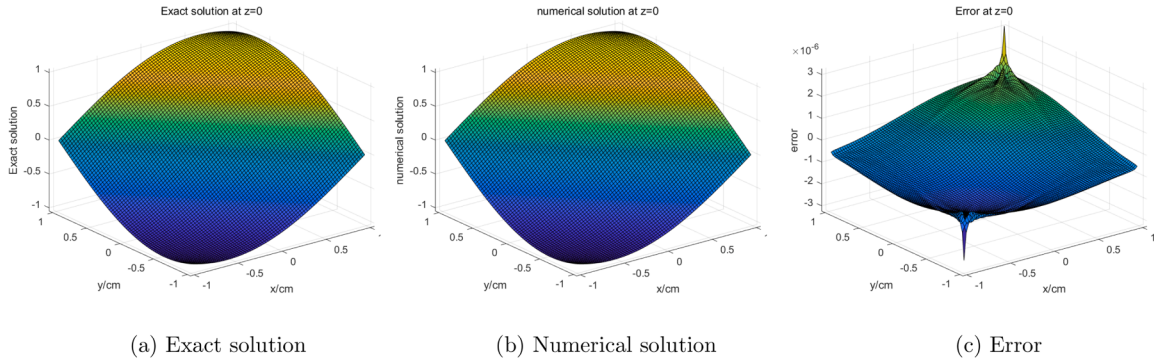


Fig. 1. Comparison between exact and numerical solution at $z = 0$.

Table 2
 L^2 error and L^∞ error on different spatial size.

N	L^2 error	Order	L^∞ error	Order
10	9.9925E-03	–	5.3974E-03	–
20	2.4475E-03	2.0295	1.3288E-03	2.0222
40	6.0489E-03	2.0166	3.2796E-04	2.0185
80	1.5096E-04	2.0025	8.1294E-05	2.0123

The numerical solution slices at $z = 0$ under spatial discrete size $h = 0.025$ are shown in Fig. 1 and the corresponding L^2 error and L^∞ error at different spatial discrete sizes are shown in Table 2. From Table 2, we observe that the L^2 and L^∞ error both decrease with second-order accuracy as the spatial size becomes smaller. This result is consistent with the theoretical expectations, indicating that the code can be applied effectively in real-world scenarios.

4.2. Material redefinition in spatial adaptive mesh

In spatial discretization, adaptive mesh technology is employed to enhance precision and efficiency. In the fourth step of the adaptation process outlined in Algorithm 2, we redefine the material properties of the voxels within the spatial mesh. Before proceeding with this step, it is crucial to establish the importance of material redefinition in spatial adaptive discretization. To demonstrate this, we compare material representations at different depths, emphasizing the distinctions between using material redefinition and not using it. As illustrated in Figs. 2 and 3, there is a significant improvement in resolution, particularly at the boundaries, when material redefinition is applied. This clearly highlights the effectiveness of the material redefinition process.

4.3. Water models

In this paper, we consider two water models, as illustrated in Fig. 4. Specifically, the models involve a beam of photons with varying energies directed perpendicularly into a water tank. Different beam sizes correspond to different incident fields. To approximate this incident condition, we employ the following extra source term:

$$S(\vec{r}, E, \hat{\Omega}) = 10^9 \delta(\vec{r} - \vec{r}_{inc}) f(E) \delta(\hat{\Omega} - [0, 0, 1]), \quad (10)$$

where \vec{r} is located in the calculation domain D , $\vec{r}_{inc} = [-3, 3] \times [-3, 3] \times 0 \text{ cm}^3$ represents the incident field, and $f(E)$ is the energy function that characterizes the energy of the incident beam. The energy function $f(E)$ for water models which illustrated in Fig. 5 are chosen as

- Water model 1: $f(E) = \delta(E - 9.4842)$;
- Water model 2: $f(E) = E$.

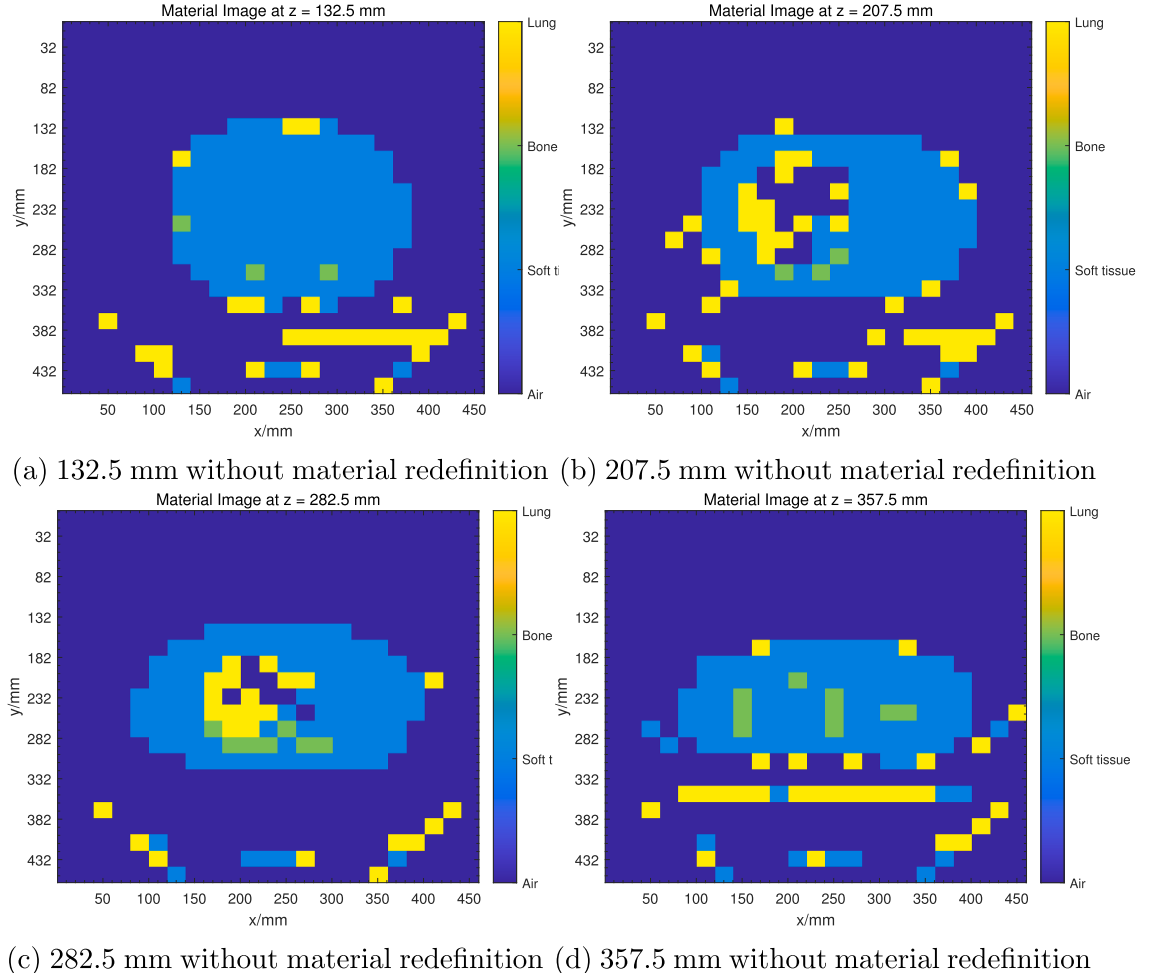


Fig. 2. Comparison on material image without material redefinition.

Table 3
Details in numerical model.

Parameters	Values
Computation domain	$[-10, 10] \times [-10, 10] \times [0, 40] \text{ cm}^3$
Field size	$[-3, 3] \times [3, 3] \text{ cm}^2$
Number of hexahedral elements	41,400
Minimum element size	$2 \times 2 \times 2 \text{ mm}^3$
Maximum element size	$1 \times 1 \times 1 \text{ cm}^3$
Angular discrete quadrature	$L - T(200)$
Legendre expansion number	$L = 5$

4.3.1. Details in models

The identical parameters in slab models are listed in **Table 3**. In $L - T(200)$, 10th order Lobatto quadrature is selected as ξ level, and 19,17,15,13,11,9,7,5,3,1th order Tschebyscheff quadrature is selected for each ξ level. For water model 2, the energy function is continuous, thus 21 photon and 20 electron energy groups are utilized, and both the photon and electron energy groups ranged from 0.001 Mega electron Volt (MeV) to 9.4842 MeV with group widths ranging from 0.00075 MeV at lower energies to 2.8442 MeV at higher energies. For water model 1, there is an extreme shock at the highest energy, so an extra group is used here for accuracy.

4.3.2. Comparison

To compare our results with the MC simulations, we employed several metrics, including depth versus percentage dose distribution (PDD) curves at the isocenter (which is calculated by averaging the dose distribution near the geometric center of the computation domain) and CT image comparisons between the two methods. The accuracy of the results is ultimately assessed using the gamma index under various formulations, a widely adopted method in clinical practice.

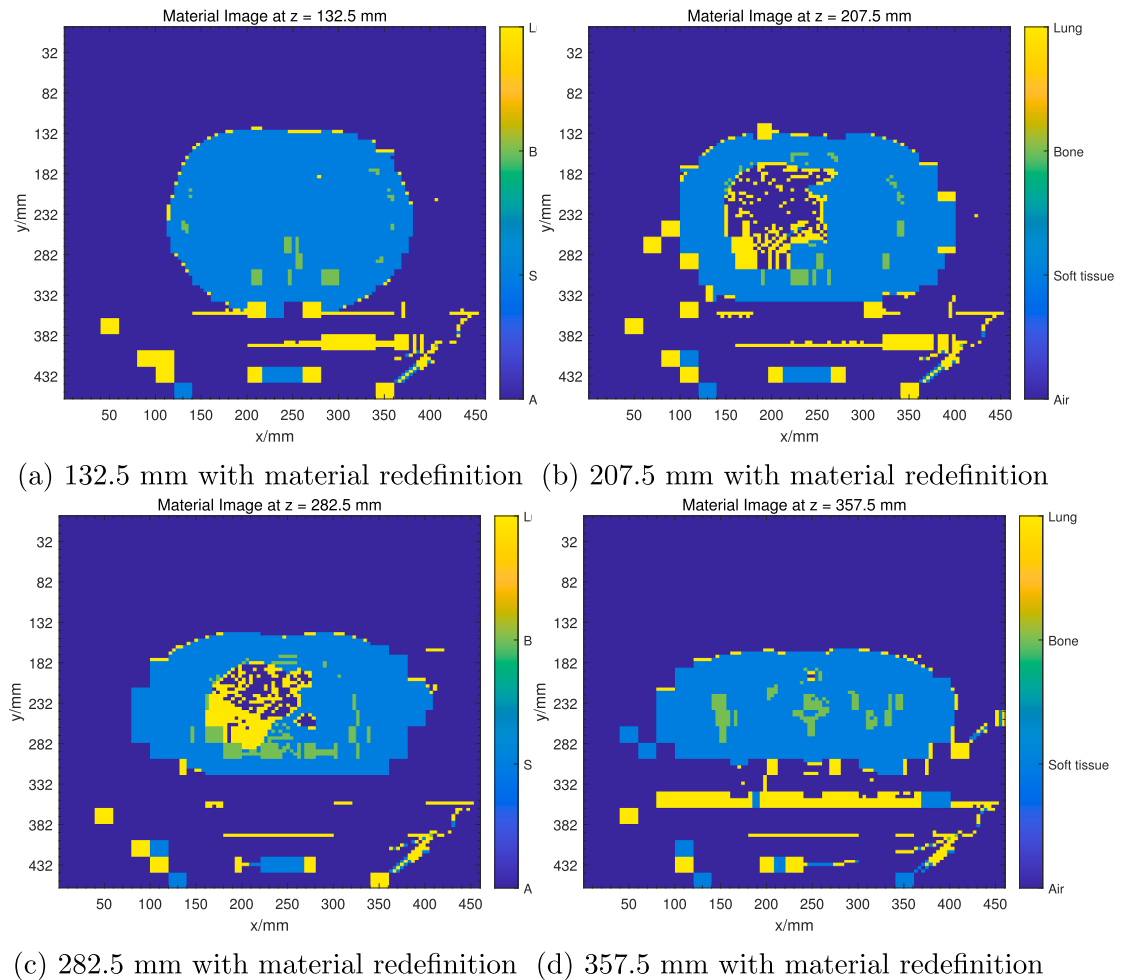


Fig. 3. Comparison on material image with material redefinition.

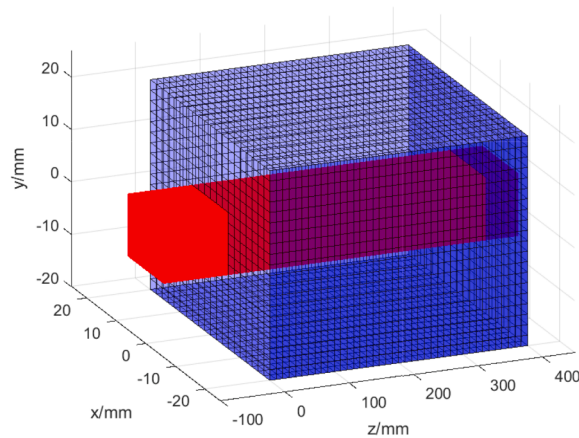


Fig. 4. Model graph(red: incident photon beam; blue: water tank). (For interpretation of the references to color in this figure legend, the reader is referred to the web version of this article.)

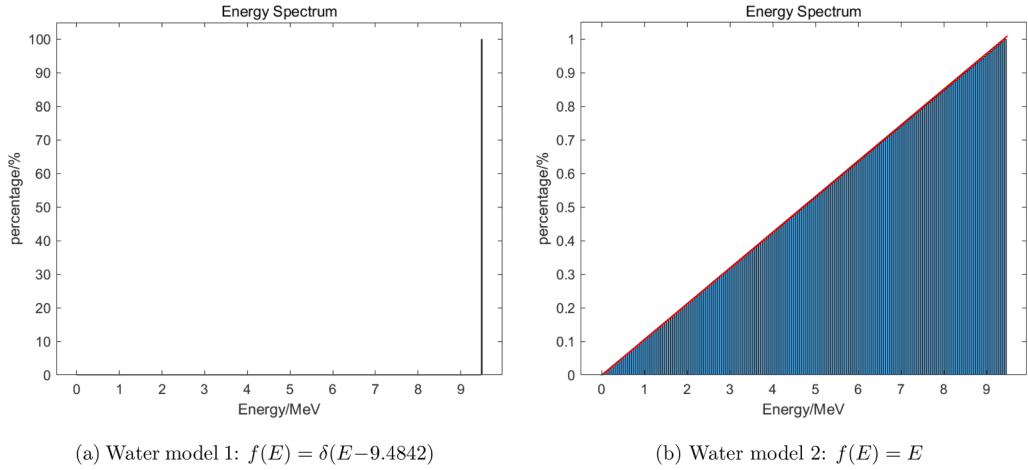
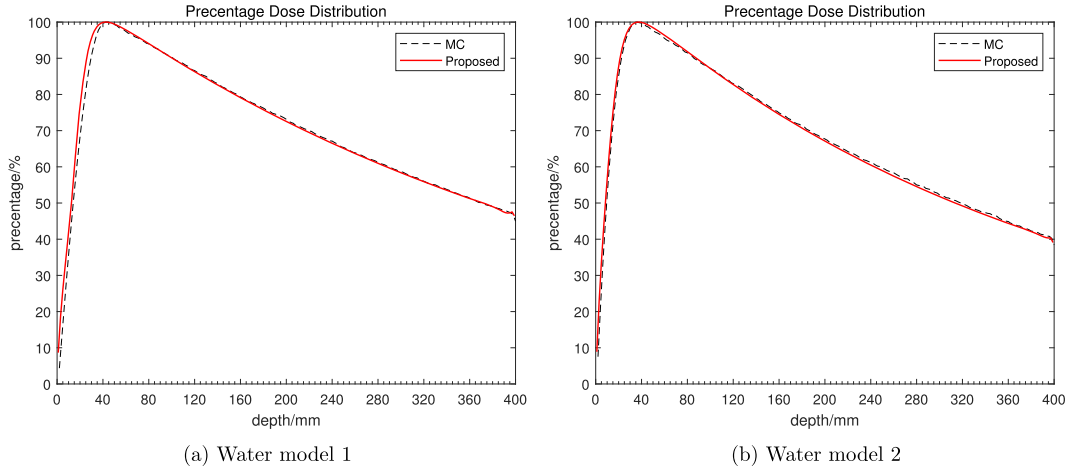
**Fig. 5.** Energy functions.**Fig. 6.** Percentage dose distribution for two water models.

Fig. 6 presents the percentage dose distribution curve for MC compared to our algorithm in the external beam benchmark for two water models. **Figs. 7** and **8** show the CT image comparisons of the two models at 151 mm. We observe a strong agreement between our results and MC references. The oscillations can be seen in the MC method, as shown in **Figs. 7** and **8**. In **Fig. 6**, the dose distribution results are presented as averages, offering a general overview of data trends. In contrast, **Figs. 7** and **8** display the results pointwise, emphasizing values at specific locations rather than averaging them. Although averaging calculations can slightly reduce these oscillations, as demonstrated in **Fig. 6**, our algorithm effectively avoids this issue entirely.

To further evaluate how accurate the two results are, gamma indices under 2% 2 mm Distance to agreement (DTA) and 2% 3 mm DTA formulations are calculated. When calculating the gamma index, only voxels whose dose is higher than 10% maximum dose in the calculation domain are considered. The detailed gamma indices and degrees of freedom (DoF) and computational time (Time) are shown in **Table 4**. From **Figs. 6**, **8** and **Table 4**, our method demonstrates significant efficiency in dose simulation, requiring fewer DoF and shorter computational time while delivering greater accuracy than the MC method. Additionally, the MC method displays oscillatory behavior at the tail of the dose distribution, a phenomenon that is not present in our approach. To better illustrate the efficiency of our algorithm, we also include the non-adaptive method in the comparison, which utilizes $5 \times 5 \times 5 \text{ mm}^3$ hexahedral elements and $L-T(288)$ quadrature for spatial and angular discretization. In comparison, the non-adaptive method requires approximately four times the degrees of freedom (DoF) and computational time to achieve results equivalent to those obtained with our algorithm for these two water models.

4.4. Slab models

To further test our algorithm, we compute two slab models to assess its ability to calculate dose in anisotropic materials. Each slab model consists of a spatial domain that includes three different materials.

Table 4
Comparison between LBT and MC for two water models.

Model	Method	DoF	Time(s)	DTA	Gamma index (%)
Model 1	Adaptive LBT	3.5604E + 8	3.2264E + 3	3 mm	98.9100
				2 mm	96.2721
	Non-adaptive LBT	1.5852E + 9	1.4222E + 4	3 mm	98.9074
				2 mm	96.5616
	MC	1.0000E + 9	1.2469E + 4	3 mm	83.6903
				2 mm	72.6360
Model 2	Adaptive LBT	3.3948E + 8	7.5722E + 3	3 mm	98.4866
				2 mm	94.8950
	Non-adaptive LBT	1.5114E + 9	1.4768E + 4	3 mm	98.3967
				2 mm	95.0076
	MC	1.0000E + 9	1.6734E + 4	3 mm	72.7637
				2 mm	65.4131

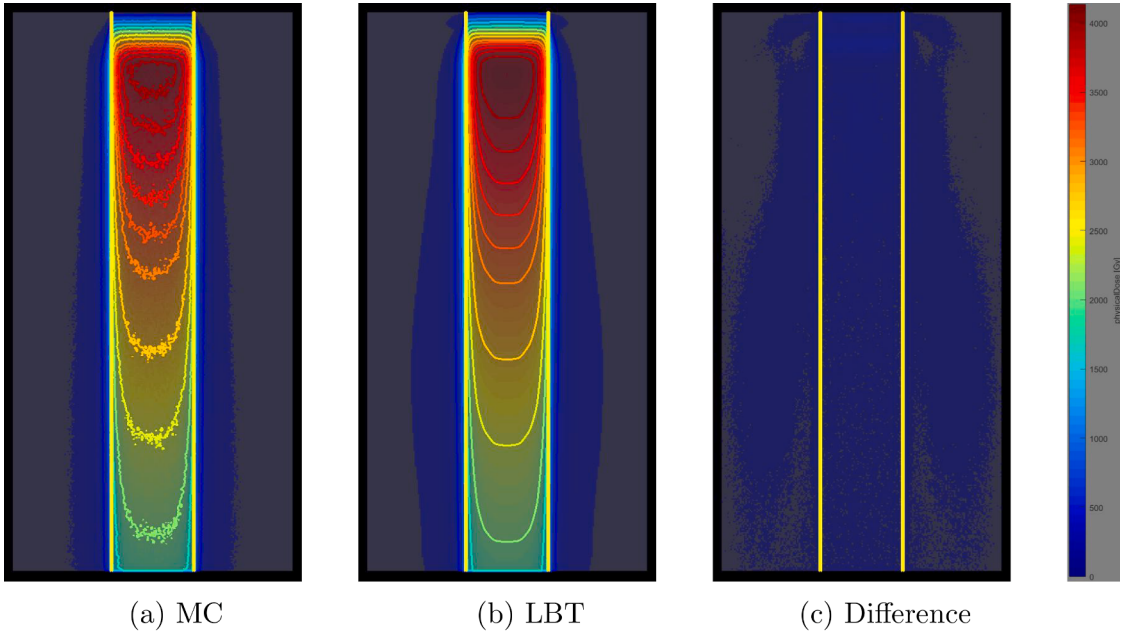


Fig. 7. CT image for water model 1 at 151 mm.

4.4.1. Details in models

The calculation parameters in slab models are listed in Table 5. In $L - T(200)$, 10th order Lobatto quadrature is selected as ξ level, and 19,17,15,13,11,9,7,5,3,1th order Tschebyscheff quadrature is selected for each ξ level. The incident energy for two different cases in slab models is the following

- Slab model 1: $f(E) = \delta(E - 9.4842)$;
- Slab model 2: $f(E) = E$.

The same energy group structure is chosen as in the corresponding water models. Regarding spatial discretization, each slab contains three different materials, and the cross sections σ_t and σ_s vary with the materials. As a result, the dose distribution will exhibit significant changes at the slab boundaries. To address this, adaptive refinement is used near the slab interfaces. Additionally, the dose distribution also varies sharply at the boundaries of the incident field, necessitating mesh refinement on both sides of the field boundaries.

4.4.2. Comparison

As two water models, the incident photon beam is monoenergetic in slab model 1, while it is multi-energetic in slab model 2. Both beams are directed perpendicularly into the slab domain for two slab models. Figs. 9 and 10 are incident energy spectrum and PDD curves of the MC method versus our method for the external beam benchmark for two slab models. The corresponding CT images at 151 mm are shown in Figs. 11 and 12, respectively. Gamma indices under difference formulations are shown in Table 6. For these two models, the relative residual errors between the two results at the isocenter are as in Fig. 13.

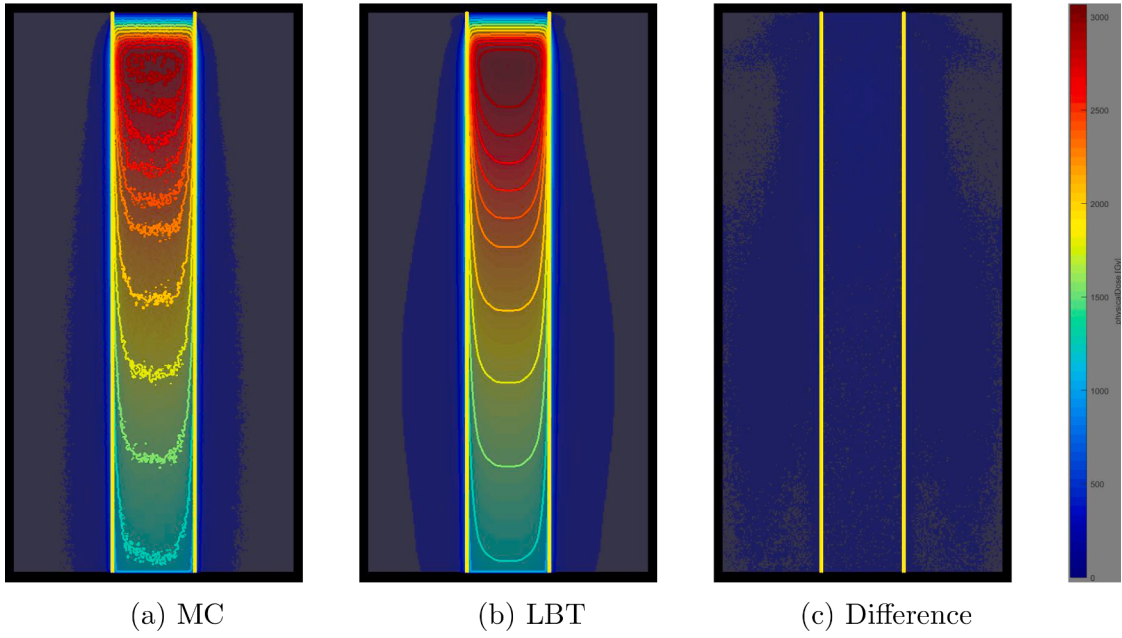


Fig. 8. CT image for water model 2 at 151 mm.

Table 5
Parameters in slab models.

Parameters	Values
Computation domain	$[-10, 10] \times [-10, 10] \times [0, 40] \text{ cm}^3$
Field size	$[-3, 3] \times [-3, 3] \text{ cm}^2$
	0 ~ 6 cm Water
Slab material	6 ~ 10 cm Bone
	10 ~ 24 cm Lung
	24 ~ 40 cm Water
Number of hexahedral elements	64,800
Minimum element size	$2 \times 2 \times 2 \text{ mm}^3$
Maximum element size	$1 \times 1 \times 1 \text{ cm}^3$
Angular discrete quadrature	$L - T(200)$
Legendre expansion number	$L = 5$

Table 6
Comparison between LBT and MC for two slab models.

Model	Method	DoF	Time (s)	DTA	Gamma index (%)
Model 1	Adaptive LBT	1.1449E + 9	4.8955E + 3	3 mm 2 mm	94.0646 92.3638
	Non-adaptive LBT	1.2681E + 10	5.2726E + 4	3 mm 2 mm	94.6034 92.8651
	MC	1.0000E + 10	1.2968E + 4	3 mm 2 mm	77.9159 70.4278
Model 2	Adaptive LBT	1.0916E + 9	6.8024E + 3	3 mm 2 mm	95.4825 92.8794
	Non-adaptive LBT	1.20914E + 10	6.9003E + 4	3 mm 2 mm	96.0661 92.6762
	MC	1.0000E + 10	1.7453E + 4	3 mm 2 mm	64.1107 58.1860

From Figs. 9 to 13 and Table 6, our method demonstrates high efficiency in dose simulation, exhibiting lower DoF, shorter computational time and superior accuracy compared to the MC method. Although the oscillation in the MC results appeared to decrease by 10 times particle simulation, it nevertheless persisted. For the non-adaptive method, $2.5 \times 2.5 \times 2.5 \text{ mm}^3$ hexahedral elements and $L-T(288)$ quadrature are employed for spatial and angular discretization. This method requires approximately ten times the DoF and computational time to achieve results equivalent to those obtained with our algorithm for these two slab models.

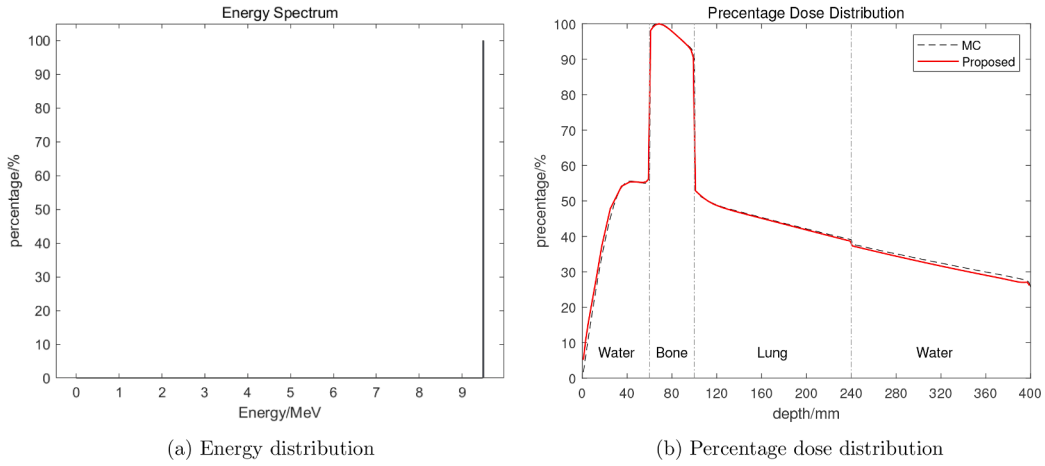


Fig. 9. Energy spectrum and percentage dose distribution in slab model 1.

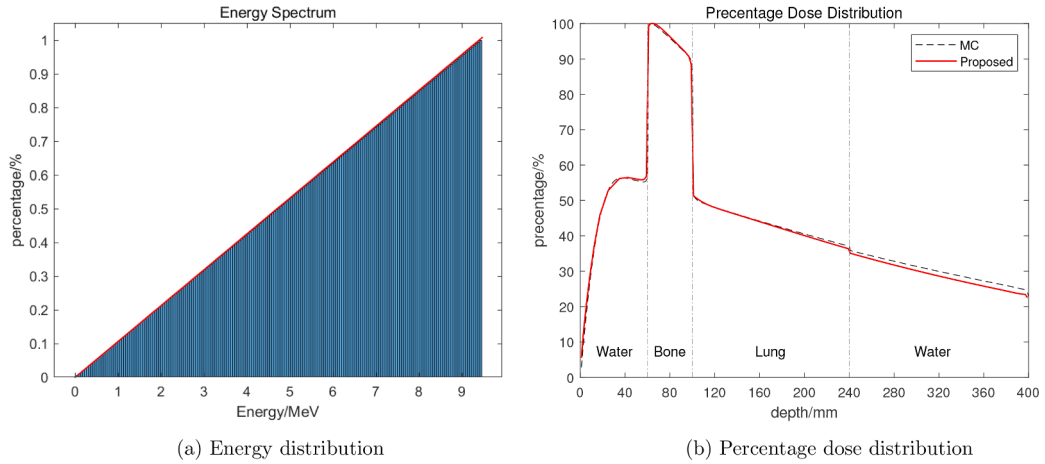


Fig. 10. Energy spectrum and percentage dose distribution in slab model 2.

Table 7
Parameters in patient models.

Parameters	Values
Computation domain	$[-30, 27.5] \times [-24.18, 33.32] \times [12, 37] \text{ cm}^3$
Field size	$[-2.5, 2.5] \times [-1.68, 3.32] \text{ cm}^2$
Number of hexahedral elements	87,394
Minimum element size	$2 \times 2 \times 2 \text{ mm}^3$
Maximum element size	$2 \times 2 \times 2 \text{ cm}^3$
Angular discrete quadrature	$L - T(310)$
Legendre expansion number	$L = 5$

4.5. Patient model

Finally, we simulate a model based on a patient's data from a lung CT image. In this example, the material composition within the computational domain becomes considerably more intricate than that observed in the water and slab models presented above. This allows us to test the efficiency of our algorithm in real-world applications.

4.5.1. Details in models

The calculation parameters in patient models are listed in Table 7. In $L - T(310)$, 12th order Lobatto quadrature is selected as ξ level, and 24,22,20,18,16,14,12,10,8,6,4,1th order Tschebyscheff quadrature is selected for each ξ level. The incident energy in patient model is the following

- Patient model: $f(E) = E$.

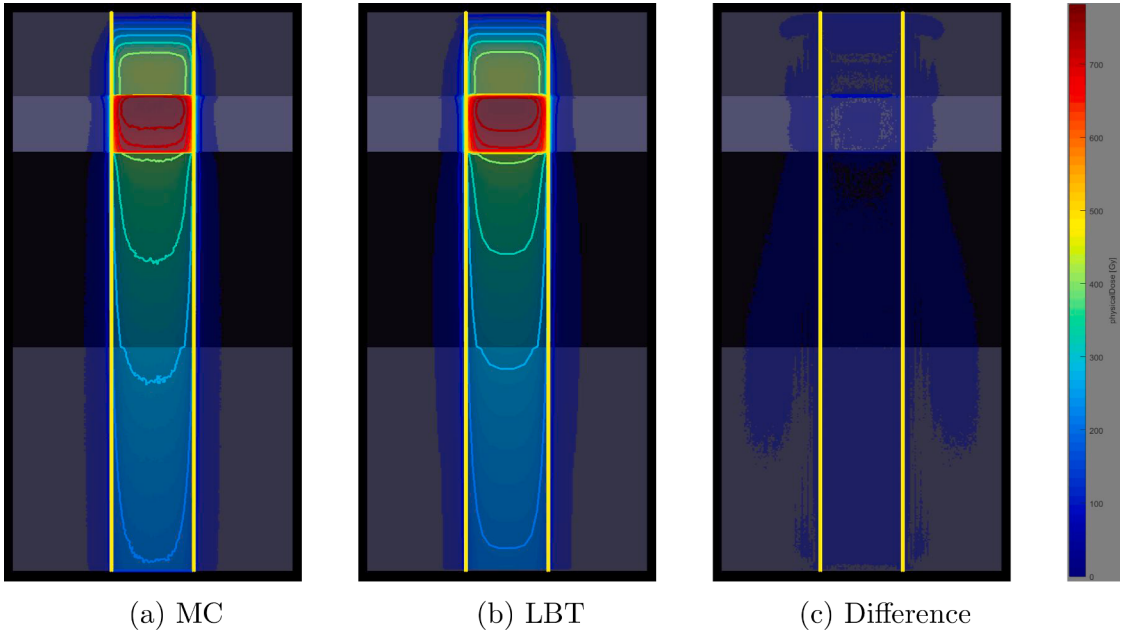


Fig. 11. CT image for slab model 1 at 151 mm.

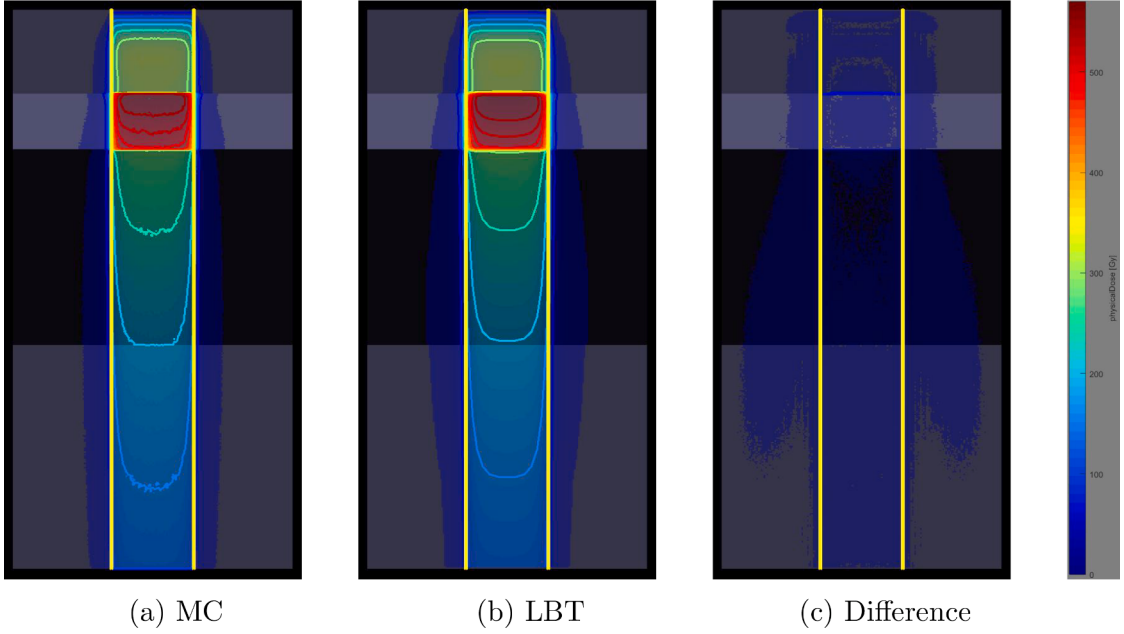


Fig. 12. CT image for slab model 2 at 151 mm.

The same energy group structure is chosen as in the corresponding water and slab models. For each voxel, the average Hounsfield units is calculated before assigning a material to that voxel. Based on this average Hounsfield units, the voxel material is classified as air, lung, soft tissue, or bone. The conversion in [Table 8](#) from Hounsfield units to material is determined through visual examination of the CT image. The adaptive mesh image slices are shown in [Fig. 14](#).

4.5.2. Comparison

The patient model represents a spectrum model, with an incident photon beam that is multi-energetic and directed perpendicularly into the patient domain. [Fig. 15](#) displays the incident energy spectrum alongside a PDD curve, comparing the MC method with our

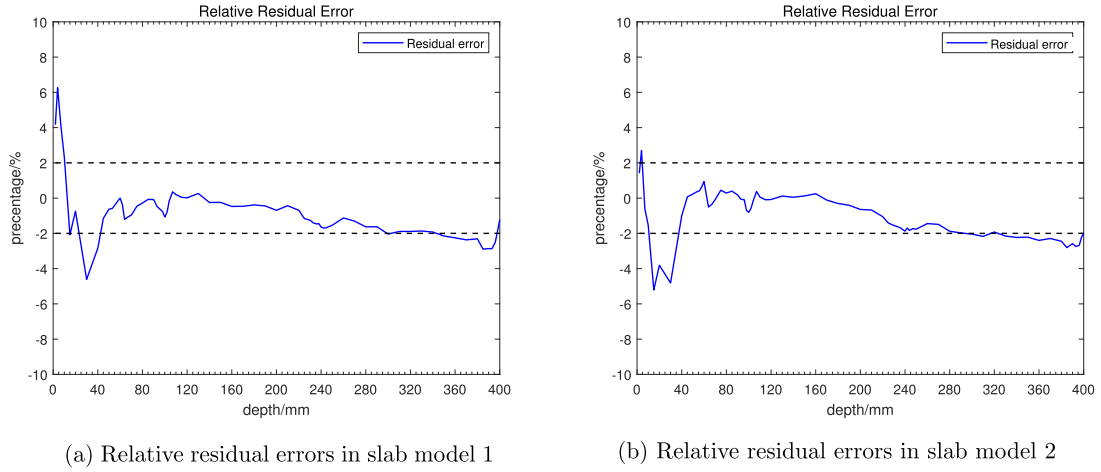


Fig. 13. Relative Residual Errors between two results for slab model 1 and slab model 2.

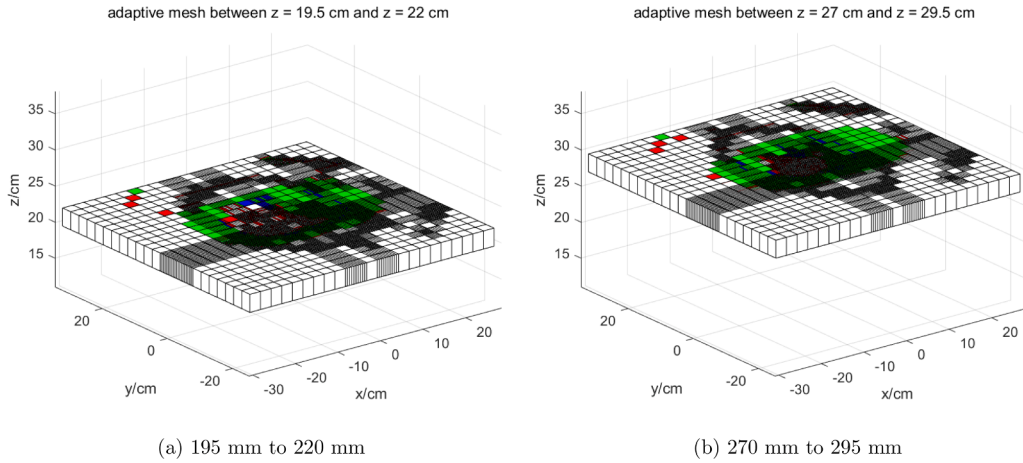


Fig. 14. Adaptive mesh image at different depths (white: air, red: lung, green: soft tissue, blue: bone). (For interpretation of the references to color in this figure legend, the reader is referred to the web version of this article.)

Table 8
Conversion from Hounsfield units to material for the anthropomorphic phantom.

Hounsfield units range	Material	Density (g cm^{-3})
Less than -853	Air	1.2048×10^{-3}
From -853 to -154	Lung	1.04
From -153 to 101	Soft tissue	1
Greater than 101	Bone	1.85

algorithm for the external beam benchmark in the patient model. The CT images at 145 mm are shown in Figs. 16 and 17 from two different perspectives. Simultaneously, we also calculate the gamma index under different formulations in Table 9. From Figs. 15 to 17 and Table 9, our method still has significant advantages over the MC method. The DoF of the MC method is up to 10^{10} while it's only about 10^9 for our algorithm and our algorithm uses only 2/3 of the computational time compared to the MC method. Additionally, we observe a significant increase in each gamma index, indicating that adaptive mesh refinement in Algorithm 2 is an effective tool for enhancing the alignment between our method and the MC results. As for the non-adaptive method, $2 \times 2 \times 2 \text{ mm}^3$ hexahedral elements and $L - T(440)$ quadrature are used in spatial and angular discretization and it needs too much DoF and computational time to get equivalent level results as our algorithm for this patient model.

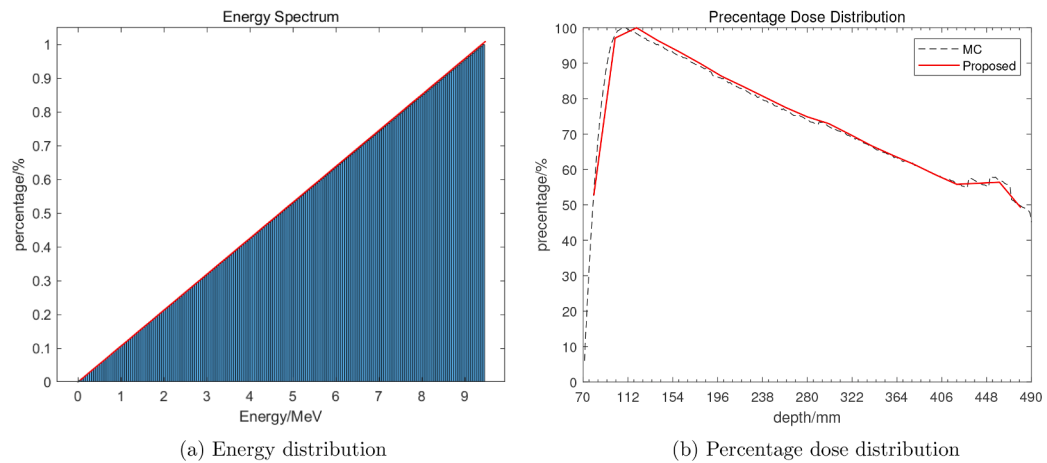


Fig. 15. Energy distribution and result comparison in patient model.

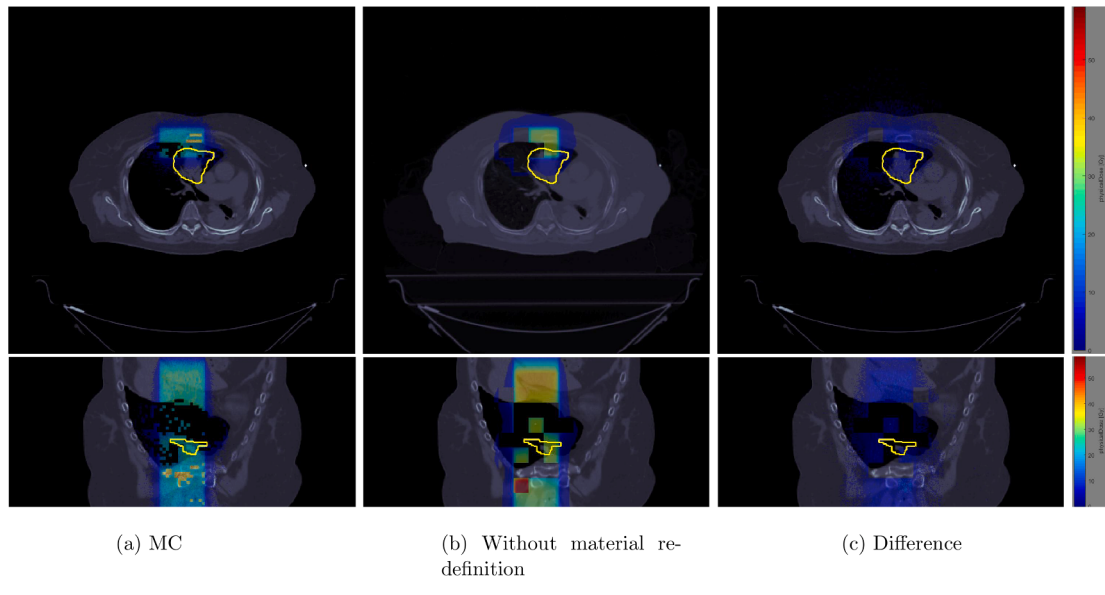


Fig. 16. CT image for patient model at 145 mm.

Table 9
Comparison between our result and MC for patient model.

Material Handling	Method	Dof	Time (s)	DTA	Gamma index (%)
With material redefinition	Adaptive LBT	4.4431E+9	1.0034E+5	3 mm 2 mm	99.8780 97.7638
			1.4569E+5	3 mm 2 mm	85.5976 73.8589
	MC	1.0000E+10	1.0263E+5	3 mm 2 mm	99.3427 91.7397
			>1E+6	3 mm 2 mm	\ \
Without material redefinition	Non-adaptive LBT	>1E+11	>1E+6	3 mm 2 mm	69.3563
	MC	1.0000E+10	1.4378E+5	3 mm 2 mm	55.5732
			>1E+6	>1E+6	>1E+6

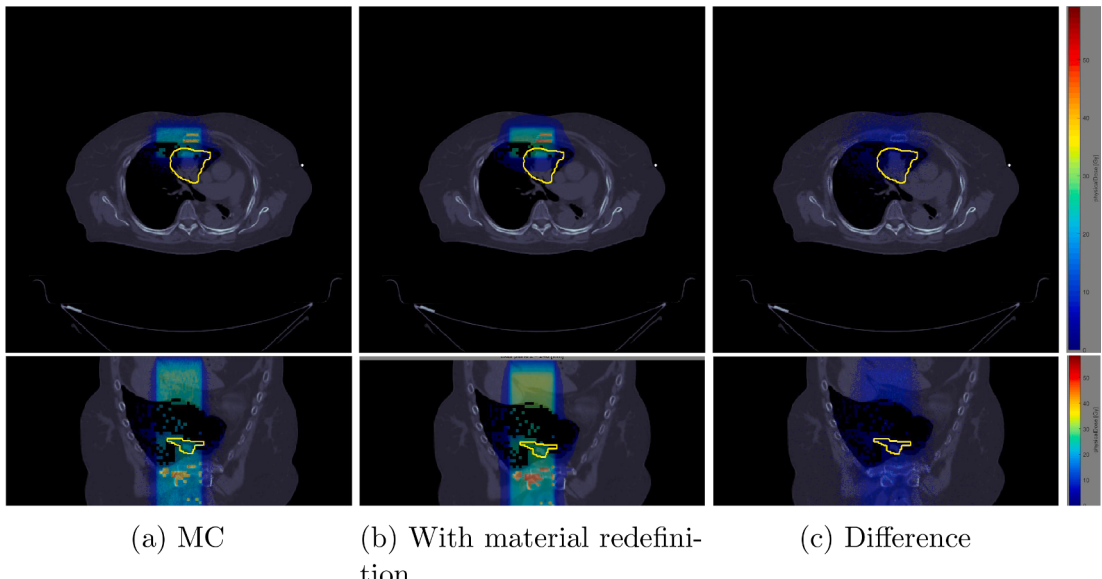


Fig. 17. CT image for patient model at 145 mm.

5. Conclusion and outlook

In this paper, an angle and space adaptive method for the photon-electron coupled Boltzmann transport equations is proposed to solve the dose distribution in radiotherapy. The numerical scheme combines the multigroup method, $L - T$ method and DG method for energy, angular and space discretization. The overall efficiency of this algorithm is determined using one numerical, two water and two slab models. Finally, it is placed on a patient model and again performs well. In comparison to the MC method, our algorithm has lower DoF, shorter computational time and higher accuracy. Our algorithm achieves excellent agreement with the benchmark from the MC method, with the gamma index reaching at least 92 % and 95 % at 2%/2 mm DTA criteria and 2%/3 mm DTA criteria, respectively, for all test models.

In future studies, we will try to apply our algorithms to a wider range of clinically relevant cases, especially cases where the presence of some local heterogeneity, small fields, sharp edges, and high density gradients can make computation difficult. And we will also try to build on this work to propose some acceleration techniques that can be applied to a wider range of clinical models to really speed up dose calculation in clinical applications.

CRediT authorship contribution statement

Xilin Zhang: Writing – review & editing, Writing – original draft, Visualization, Validation, Software, Methodology, Formal analysis, Data curation; **Peimeng Yin:** Writing – review & editing, Methodology, Conceptualization; **Xue Hong:** Writing – review & editing, Visualization; **Wei Wu:** Data curation; **Wangyao Li:** Data curation; **Yuxin Wang:** Data curation; **Yan Xu:** Writing – review & editing, Supervision, Project administration, Methodology, Funding acquisition, Conceptualization; **Hao Gao:** Writing – review & editing, Supervision, Project administration, Methodology, Conceptualization.

Data availability

Data will be made available on request.

Funding

Research of Peimeng Yin is supported by the University of Texas at El Paso Startup Award. Research of Xue Hong and Hao Gao are partially supported by the NIH grants Nos. R37CA250921, R01CA261964. Research of Yan Xu is supported by NSFC grant 12471347.

Declaration of competing interest

The authors declare that they have no known competing financial interests or personal relationships that could have appeared to influence the work reported in this paper.

References

- [1] M.E. Carrington, S. Mrówczyński, Transport theory beyond binary collisions, Phys. Rev. D 71 (2005) 065007. <https://doi.org/10.1103/PhysRevD.71.065007>
- [2] L. Minafra, F.P. Cammarata, M. Calvaruso, The role of radiation in cancer treatment: new insights towards personalized therapies, J. Pers. Med. 12 (2022) 312. <https://doi.org/10.3390/jpm12020312>
- [3] H. Hensel, R. Iza-Teran, N. Siedow, Deterministic model for dose calculation in photon radiotherapy, Phys. Med. Biol. 51 (2006) 675–693. <https://doi.org/10.1088/0031-9155/51/3/013>
- [4] K. Gifford, J. Horton, T. Wareing, G. Failla, F. Mourtada, Comparison of a finite-element multigroup discrete-ordinates code with Monte Carlo for radiotherapy calculations, Phys. Med. Biol. 51 (2006) 2253–2265. <https://doi.org/10.1088/0031-9155/51/9/010>
- [5] J. St-Aubin, A. Keyvanloo, O. Vassiliev, B. Fallone, A deterministic solution of the first order linear Boltzmann transport equation in the presence of external magnetic fields, Med. Phys. 42 (2015) 780–793. <https://doi.org/10.1118/1.4905041>
- [6] J. St-Aubin, A. Keyvanloo, B. Fallone, Discontinuous finite element space-angle treatment of the first order linear Boltzmann transport equation with magnetic fields: application to MRI-guided radiotherapy, Med. Phys. 43 (2016) 195–204. <https://doi.org/10.1118/1.4937933>
- [7] O. Zelyak, B. Fallone, J. St-Aubin, Stability analysis of a deterministic dose calculation for MRI-guided radiotherapy, Phys. Med. Biol. 63 (2017) Paper No.015011. <https://doi.org/10.1088/1361-6560/aa959a>
- [8] R. Yang, D.M. Santos, B.G. Fallone, J. St-Aubin, A novel transport sweep architecture for efficient deterministic patient dose calculations in MRI-guided radiotherapy, Phys. Med. Biol. 64 (2019) 185012. <https://doi.org/10.1088/1361-6560/ab35bc>
- [9] A. Swan, Y. Ray, O. Zelyak, J. St-Aubin, Feasibility of streamline upwind Petrov-Galerkin angular stabilization of the linear Boltzmann transport equation with magnetic fields, Biomed. Phys. Eng. Express 7 (2020) Paper No.015017. <https://doi.org/10.1088/2057-1976/abd239>
- [10] V.P. DeCaria, C.D. Hauck, S.R. Schnake, An asymptotic preserving discontinuous Galerkin method for a linear Boltzmann semiconductor model, SIAM J. Numer. Anal. 62 (2024) 1067–1097. <https://api.semanticscholar.org/CorpusID:269622778>.
- [11] M. Ghattassi, J.R. Roche, F. Asllanaj, M. Boutayeb, Galerkin method for solving combined radiative and conductive heat transfer, Int. J. Therm. Sci. 102 (2016) 122–136. <https://api.semanticscholar.org/CorpusID:123804489>.
- [12] W. Han, J. Huang, J.A. Eichholz, Discrete-ordinate discontinuous Galerkin methods for solving the radiative transfer equation, SIAM J. Sci. Comput. 32 (2010) 477–497. <https://api.semanticscholar.org/CorpusID:10358044>.
- [13] P. Houston, M.E. Hubbard, T.J. Radley, O.J. Sutton, R.S.J. Widdowson, Efficient high-order space-angle-energy polytopic discontinuous Galerkin finite element methods for linear Boltzmann transport, J. Sci. Comput. 100 (2023). <https://api.semanticscholar.org/CorpusID:258212899>.
- [14] D.A. Low, W.B. Harms, S. Mutic, J.A. Purdy, A technique for the quantitative evaluation of dose distributions, Med. Phys. 25 (1998) 656–661. <https://api.semanticscholar.org/CorpusID:20476747>.
- [15] L.J. Lorence, J.E. Morel, G.D. Valdez, Physics guide to CEPXS: a multigroup coupled electron-photon cross-section generating code, 1989. <https://api.semanticscholar.org/CorpusID:115389909>.